Formation and stability of dense arrays of Au nanoclusters on hexagonal boron nitride/Rh(111)

Matthew C. Patterson,[1] Bradley F. Habenicht,[2] Richard L. Kurtz,[1] Li Liu,[3] Ye Xu,[4] and Phillip T. Sprunger[1]
[1]*Department of Physics and Astronomy, Louisiana State University, Baton Rouge, Louisiana 70803, USA*
[2]*Department of Chemistry and Chemical Biology, University of California, Merced, Merced, California 95343, USA*
[3]*Department of Materials Science and Engineering, Texas A&M University, College Station, Texas 77843, USA*
[4]*Department of Chemical Engineering, Louisiana State University, Baton Rouge, Louisiana 70803, USA*
(Received 1 April 2014; published 20 May 2014)

We have studied the nucleation and growth of Au clusters at submonolayer and greater coverages on the *h*-BN nanomesh grown on Rh(111) by means of scanning tunneling microscopy (STM), x-ray photoelectron spectroscopy (XPS), and density functional theory (DFT). STM reveals that submonolayer Au deposited at 115 K nucleates within the nanomesh pores and remains confined to the pores even after warming to room temperature. Whereas there is a propensity of monoatomic high islands at low temperature, upon annealing, bi- and multilayer Au clusters emerge. Deposition of higher coverages of Au similarly results in Au clusters primarily confined to the nanomesh pores at room temperature. XPS analysis of core-level electronic states in the deposited Au shows strong final-state effects induced by restricted particle size dominating for low Au coverage, with indications that larger Au clusters are negatively charged by interaction through the *h*-BN monolayer. DFT calculations suggest that the structure of the Au clusters transitions from monolayer to bilayer at a size between 30 and 37 atoms per cluster, in line with our experiment. Bader charge analysis supports the negative charge state of deposited Au.

DOI: 10.1103/PhysRevB.89.205423 PACS number(s): 68.43.Hn, 73.22.−f

I. INTRODUCTION

Although bulk gold is one of the least reactive (noblest) metals [1], it is by now well established that Au clusters supported on various metal oxides show strong catalytic activity for a wide variety of oxidation reactions. In particular, the low-temperature oxidation of CO by molecular O_2 has been observed to occur for Au nanoparticles on oxide supports [2–5]. The most dramatic and well-known factor known to influence the catalytic activity of such systems is the size and shape of the Au nanoparticles, with catalytic properties virtually absent for particles larger than a few nm^3. In addition to particle size, charge transfer between the support and Au clusters, particularly dependent on the dimensionality of the cluster, plays a key role in the adsorption of reactants and the selectivity of reactions [2,6–9]. Cluster nucleation and charge transfer are often facilitated by defects in the support [10–12]. These experimental findings underlie the key idea that the choice of support exerts critical influence over the nucleation, morphology (size, shape, and distribution), charge state, and other properties of deposited metal clusters, and Au catalysts can almost never be considered in isolation of the support.

One possibility for tailoring the size, shape, and distribution of Au nanoparticles for catalytic reactions of interest is through deposition onto a patterned substrate. Hexagonal boron nitride (*h*-BN) monolayers grown epitaxially on single-crystal transition metal surfaces show unique promise as such a template for various reasons. First, the growth of single-layer *h*-BN on transition metal surfaces by pyrolysis of borazine is easily accomplished [13], and the self-limiting nature of the growth process guarantees precise control of the *h*-BN film thickness and morphology. The resulting monolayer films show thermal stability and chemical inactivity up to 600 °C [14]. Furthermore, *h*-BN monolayers can form a variety of self-assembled nanostructures that vary with the choice of transition metal substrate, from a (1×1) monolayer on Ni(111) [15] to a highly corrugated superstructure on Rh(111) and Ru(0001) [13,16,17]. In general, the binding of *h*-BN to transition metal surfaces is influenced by the lattice match of the metal surface and the *h*-BN film and the degree of hybridization between metal *d* bands and *h*-BN π^* bands [18–23]. Hence, Ni(111), which has a nearly perfect lattice match to the *h*-BN and partially unfilled *d* bands, shows a relatively strongly bound commensurate *h*-BN monolayer [24], while Cu(111) shows a much weaker binding of the *h*-BN monolayer [18]. Of the 4*d* elements, Ru(0001) and Rh(111) have a large lattice mismatch to the *h*-BN (8.2% and 7.6%, respectively), but unfilled *d* bands that should result in strongly bound *h*-BN layers. Finally, *h*-BN on transition metal surfaces is free of oxygen and can help avoid ambiguities in the interpretation of the nature of active sites in CO oxidation on Au nanocatalysts [25–27].

Thus, rather than adopting a strongly bound (1×1) monolayer, the *h*-BN films grown on these 4*d* surfaces adopt what has become widely referred to as a "nanomesh" structure, with hexagonal "pores" of diameter 2 nm surrounded by "wires" sitting farther away from the Rh surface, with an overall periodicity of 3.2 nm, corresponding to a unit cell consisting of a 12×12 substrate against a 13×13 *h*-BN superstructure [16,28]. Spectroscopic techniques show splitting of the *h*-BN σ and π bands [29] and of core-level N 1*s* and B 1*s* states [22] of the nanomesh on both Ru(0001) and Rh(111), which was initially attributed to the formation of an *h*-BN double layer [13], but was later recognized to be a consequence of the "nanomesh" structure of an *h*-BN monolayer [16,30]. As a result of the preference for strong binding to the metal surface competing with the lattice mismatch, the strongly bound *h*-BN "pore" regions are in fact chemically distinct from the "wire" regions. The resulting periodic structure of varying chemical environments provides a template that may facilitate the nucleation of nanoparticles on the order of the pore size. Buffer layer assisted growth has been used to deposit Co nanoparticles in such a fashion, with the resulting nanoparticles shown to be electronically decoupled from the

underlying Rh(111) [31,32]. A comprehensive understanding of how the deposition and growth conditions affect the size and number density of metal nanoclusters formed on template surfaces can lead to an entire class of new nanomaterials suited for model catalytic studies [33–35].

Goriachko *et al.* studied the formation of larger Au clusters on *h*-BN/Ru(0001) with STM, observing at room temperature both the nucleation of clusters in the pores and the formation of larger two-dimensional islands that extend over several pores and display the same pore-wire corrugation as the nanomesh [30], akin to the two-dimensional (2D) Au islands formed on graphene moiré/Ru(0001) [36,37]. Ng *et al.* used synchrotron-based angle-resolved photoemission spectroscopy, x-ray photoelectron spectroscopy (XPS), and near-edge x-ray-absorption fine structure (NEXAFS) spectroscopy to probe submonolayer Au on *h*-BN/Rh(111) deposited at room temperature and annealed up to 875 K, inferring nucleation of 2D Au clusters within the *h*-BN pores at room temperature, diffusion of Au between pores resulting in the formation of three-dimensional (3D) clusters starting at 575 K, and eventual Au-Rh surface alloying at 875 K [38]. DFT studies of single- and few-atom Au clusters in the *h*-BN nanomesh show a strong preference for an Au adatom to bind in the pores [39], with very high barriers to diffusion between pores [39] and a net negative charge on the Au clusters [40]. So far, multiatom Au clusters have yet to be directly modeled and optimized on the full *h*-BN/Rh(111) pore-wire structure using DFT.

In this work, we examine the templated nucleation and growth of Au nanoclusters on the *h*-BN nanomesh supported on Rh(111) using STM and XPS, and present large-scale DFT calculations of several Au clusters ($\leqslant$51 atoms) supported on the full *h*-BN/Rh(111) pore-wire unit cell to explore details of the geometry and charge state of the clusters. In Sec. II, we describe our experimental methods and theoretical approach. Section III presents STM and XPS results of submonolayer evaporation of Au on the *h*-BN/Rh(111) surface at both room temperature and 115 K. Section IV discusses the DFT results in light of our experimental data. Our conclusions are presented in Sec. V.

II. METHODS

A. Experiment

STM and XPS experiments were performed in an ultrahigh vacuum system with a base pressure of 1×10^{-10} Torr consisting of two chambers connected by a gate valve. The sample preparation chamber is equipped with a sputter gun, low-energy electron diffraction (LEED) (Specs ErLEED 150), leak valves to dose various gases, and an Omicron VT STM XA, while the other chamber contains an Omicron XM1000 monochromatic x-ray source and SPECS PHOIBOS 150 hemispherical analyzer for high-resolution XPS experiments.

The Rh(111) single crystal was cleaned by repeated cycles of 15 min of Ne^+ sputtering and flashing by e-beam annealing to 1175 K. Surface cleanliness was monitored with LEED and XPS. After a clean surface was obtained, *h*-BN films were grown by thermal decomposition of borazine $(HBNH)_3$ (liquid in a glass tube attached to a standard leak valve, purified by several freeze-pump-thaw cycles) at a pressure of 1×10^{-7} Torr for 20 min (total dose 120 Langmuir) [13,17].This dosing procedure resulted in a complete, clean, well-ordered *h*-BN film as monitored by LEED, XPS, and STM. Films kept in UHV conditions for long periods of time proved resistant to adsorption of oxygen- or carbon-containing species within the sensitivity of XPS.

Au was evaporated on samples *in situ* in the STM from a homebuilt thermal evaporator (high-purity Au wire wrapped around a tungsten filament) installed in one of the 2 ¾″ ports in the Omicron VT STM XA system. Sample temperature during evaporation was monitored using a Pt-100 resistor mounted just above the sample stage in the STM; using the STM's liquid N_2 flow cryostat, an ultimate sample temperature of 115 K can be realized. The evaporator filament was kept warm for extended periods prior to sample cooling and Au evaporation in order to minimize outgassing and prevent physisorption of unwanted species onto the cold sample. Au dosage was calibrated by evaporating Au onto a clean Ru(0001) sample [Au on Ru(0001) is known to grow as monoatomic (1×1) islands at submonolayer coverages [41]] and determining the percentage of the Ru surface covered using STM. In the experiment sections of this work, the amount of Au deposited is thus given with respect to the density of the Ru(0001) surface ($1\ \text{ML} = 1.58 \times 10^{15}\ \text{atoms/cm}^2$).

STM experiments were performed using homemade electrochemically etched tungsten tips. The tunneling voltage and current were set to $\sim$1 V and $\sim$100 pA, respectively, to minimize interactions between the tip and Au clusters, as the tip was observed to pick up and drag clusters along the surface using lower voltages or higher currents. Ordinarily these tunneling conditions (imaging filled states in the sample) result in bright "wires" and dark "pores" appearing in images of the clean *h*-BN film, with the image contrast matching the actual geometric structure of the film; however, on occasion adsorbed species on the tip caused an observed contrast reversal, with dark wires and bright pores. (This contrast reversal is a consequence of imaging unoccupied rather than occupied states of the *h*-BN film [28].) Our observations of the height and lateral size of Au clusters were not affected by these imaging conditions, however.

XPS experiments were performed using monochromatic Al $K\alpha_1$ radiation ($h\nu = 1486.6$ eV, intrinsic linewidth 0.3 eV). For each sample, survey spectra were taken using a pass energy of 40 eV to ensure correct sample alignment and to check for any contamination. High-resolution spectra of B 1*s*, N 1*s*, and Au 4*f* peaks were recorded using a pass energy of 20 eV. Spectra were fitted using the built-in routines in CASAXPS; the details of the fits are discussed in the appropriate portions of the Results and Discussion section below.

B. Density functional theory calculations

Periodic DFT calculations were performed using the Vienna *ab initio* simulations package (VASP) [42] in the local density approximation (LDA) and generalized gradient approximation (GGA-PBE) [43], and with the van der Waals correction (optB86b vdW-DF) [44,45]. The results reported herein are primarily obtained at the latter two levels. The core electrons were described by the projector augmented-wave (PAW)

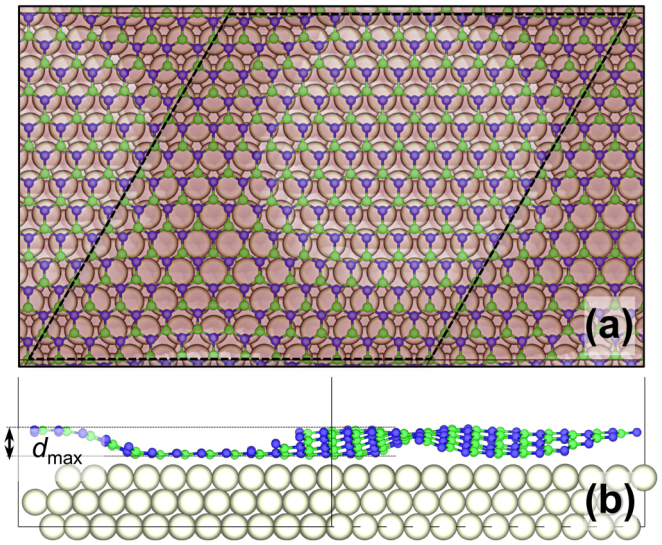

FIG. 1. (Color online) (a) Top and (b) side views of the "13-on-12" h-BN/Rh(111) pore-wire structure. The unit cell is outlined by the dashed line. White, green, and blue spheres represent Rh, B, and N atoms, respectively. More shaded areas in (a) signify greater distance of the B and N atoms from the Rh(111) substrate. The maximum corrugation height of the pore-wire structure (d_{max}) is illustrated in (b).

method [46] and the Kohn-Sham valence electrons [including Rh($4d5s$), 229 eV cutoff; Au($5d6s$), 230 eV cutoff; B($2s2p$), 319 eV cutoff; and N($2s2p$), 400 eV cutoff] were expanded in a plane wave basis set up to a cutoff energy of 400 eV. The electronic states were smeared using a first-order Methfessel-Paxton scheme with a width of 0.1 eV [47]. All total energies were extrapolated back to 0 K.

The calculated lattice constants for Rh are $a = 3.752$ Å (LDA), 3.824 Å (GGA-PBE), and 3.803 Å (optB86b vdW-DF), the last being in the closest agreement with experiment (3.80 Å [48]). The boron nitride pore-wire structure on Rh(111) was modeled using a (13×13)-h-BN monolayer on a (12×12)-Rh(111) surface unit cell ("13-on-12") depicted in Fig. 1. The Rh(111) surface was modeled as a semi-infinite three metal layer slab, for a total of 169 B, 169 N, and 432 Rh atoms in the unit cell. A vacuum space of ~16 Å was included to minimize interactions of neighboring images in the z direction. An initially flat h-BN monolayer was placed on one side of the Rh slab and relaxed into the pore-wire structure using all three exchange-correlation functionals. In the pore region of the resulting structure, the N and B atoms are located on the top of Rh atoms and over surface fcc threefold sites, respectively. During geometry optimization the BN monolayer and the top layer of Rh atoms were fully relaxed, with the bottom two layers of Rh fixed at the bulk positions. All geometric optimization was converged to 0.03 eV/Å for each relaxed degree of freedom. The reciprocal space was sampled at the Γ point only.

The adsorption of Au adatoms and clusters was studied on the BN side of the slabs only, with electrostatic decoupling in the z direction [49]. The adsorption energy (ΔE) of an Au adatom or cluster containing n Au atoms was calculated as

$$\Delta E = (E_{\text{total}} - E_{h\text{-BN/Rh(111)}} - n_{\text{Au}} E_{\text{Au}})/n_{\text{Au}},$$

where E_{total} is the energy of the overall system, $E_{h\text{-BN/Rh(111)}}$ is the energy of the clean surface without the absorbate, and E_{Au} is the energy of an Au atom in the bulk fcc metal phase. A more negative adsorption energy corresponds to stronger adsorption. Atomic charges were determined using the Bader method [50] as implemented in the code of Henkelman and co-workers [51], which partitions the total electron density into nonoverlapping atomic volumes whose surfaces are perpendicular to the electron density gradient.

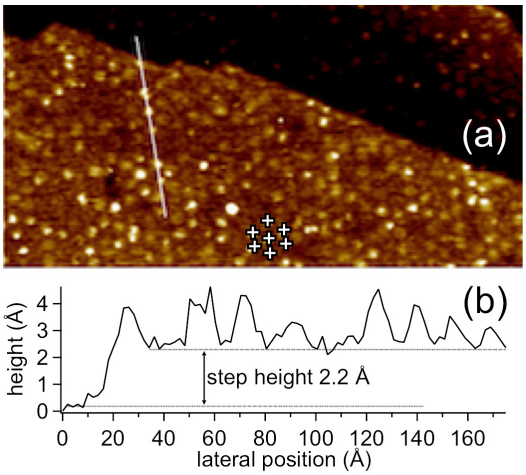

FIG. 2. (Color online) (a) 0.16 ML Au/h-BN/Rh(111) deposited at 115 K, imaged at 115 K, 500 × 250 Å^2. Tip voltage +1 V; tunneling current 100 pA. (b) Height profile along the line indicated in (a).

III. RESULTS AND DISCUSSION

A. Scanning tunneling microscopy

We begin by examining the growth of Au clusters on the h-BN/Rh(111) surface under a variety of deposition conditions, by varying the substrate temperature during deposition as well as during measurement. We first study the deposition of submonolayer amounts of Au in order to investigate the nucleation behavior of small clusters, and then turn to the deposition of larger amounts of Au in order to study the templated growth of larger nanoparticles.

Figure 2(a) shows an STM image of 0.16 ML Au deposited with the sample temperature held at 115 K, and imaged at 115 K. The line profile in Fig. 2(b) corresponds to the indicated line in the image. The step edge running diagonally from top left to middle right in the image is included in the height profile. We measure the step height as approximately 2.2 Å, taking the average difference in the z direction from the bottom of a pore on the bottom step to the bottom of a pore on the top step. This is in excellent agreement with a monatomic Rh(111) step-height distance [48]. Although the full nanomesh structure is not apparent due to tip effects, the hexagonal pore-wire structure is visible (indicated by crosses in Fig. 2). In this image, due to presumed adsorbates on the tip, pores are imaged as bright spots and wires as dark lines, as referenced in Sec. I. Au clusters in the pores are brighter

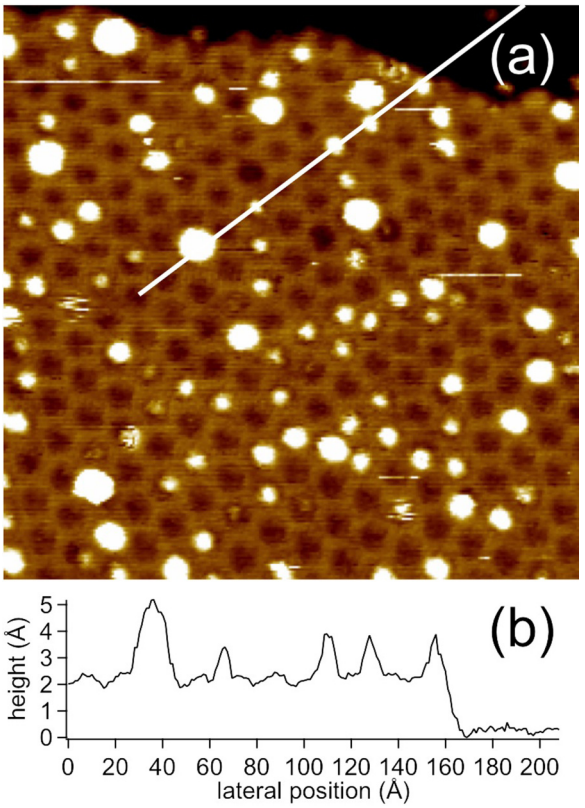

FIG. 3. (Color online) (a) 0.16 ML Au/*h*-BN/Rh(111) deposited at 115 K, imaged at 300 K, 250 × 250 Å^2. Tip voltage +1 V; tunneling current 100 pA. (b) Height profile along the line indicated in (a).

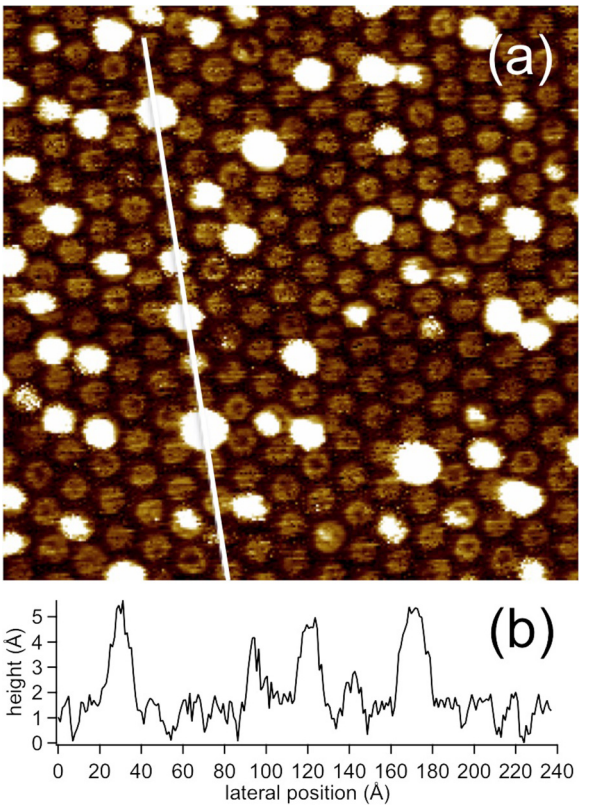

FIG. 4. (Color online) (a) 0.16 ML Au/*h*-BN/Rh(111) deposited at 300 K, imaged at 300 K, 250 × 250 Å^2. Tip voltage +1 V; tunneling current 100 pA. (b) Height profile along the line indicated above.

than the unfilled pores. The line scan across several clusters indicates that these are all approximately 1.5 Å high (relative to the bottom of a pore), indicating that they most likely consist of a single layer of Au. Under these conditions, we imaged few if any clusters that unambiguously consisted of more than one Au layer. This uniform growth mode has previously been inferred from photoemission and NEXAFS studies of similar Au coverage on *h*-BN/Rh(111) at room temperature [38]; in agreement, here we show unambiguously that after deposition at 115 K, Au exists exclusively as single-layer islands within the nanomesh pores.

Figure 3(a) shows an image of 0.16 ML Au deposited at 115 K, but warmed to room temperature before imaging. (This is the same sample as depicted in Fig. 2.) We clearly see monolayer clusters inside the pores of the *h*-BN nanomesh, as we observed exclusively at low temperature, but now larger clusters are also apparent. The image color scale has been selected to show both the pore/wire structure with corrugation 0.5 Å and the Au clusters with height 1.5–3 Å, so the difference in cluster heights is only readily apparent by examining line profiles. The indicated line scan in Fig. 3(b) shows that the small clusters still maintain the 1.5 Å height observed in the 115 K image, but additionally we see larger clusters of height 3 Å [e.g., the leftmost cluster in the profile in Fig. 3(b)], corresponding to a bilayer of Au. These bilayer clusters are also imaged as having larger lateral sizes: the bilayer cluster in Fig. 3(b) measures approximately 21 Å across compared to the 8–11 Å for the single-layer clusters in the same line scan. In this image, there also exist three clusters that appear to be even taller than a bilayer, but these populate less than 5% of the nanomesh pores.

In Fig. 3(a), we find that of the filled pores, approximately 80% are filled with single-layer clusters upon warming to room temperature, with the rest containing bilayer and the few trilayer clusters as noted above. The majority of the nanomesh pores, approximately 63%, are empty at this coverage. Raising the temperature from 115 to 300 K has evidently enabled diffusion of Au between pores, but the vast majority of the single-layer clusters presumably remain where they initially nucleated.

Figure 4(a) shows again 0.16 ML Au, but deposited and imaged at room temperature. As referenced above, presumed tip adsorbates have caused a contrast reversal in the image despite maintaining tunneling conditions identical to those in other images. The indicated line scan in Fig. 4(b) shows that typical clusters deposited at room temperature are somewhat larger than the equivalent amount of Au deposited at 115 K and warmed to room temperature. The relative occupation of single-layer versus bilayer or larger clusters is drastically different from the sample examined in Fig. 3—here approximately 40% of the clusters are single layer and 60% are bilayer or larger.

In contrast to studies of sub-ML Au/*h*-BN/Ru(0001) [28] and Au/graphene/Ru(0001) [36,37], we observe only the nucleation of small clusters confined to the nanomesh pores,

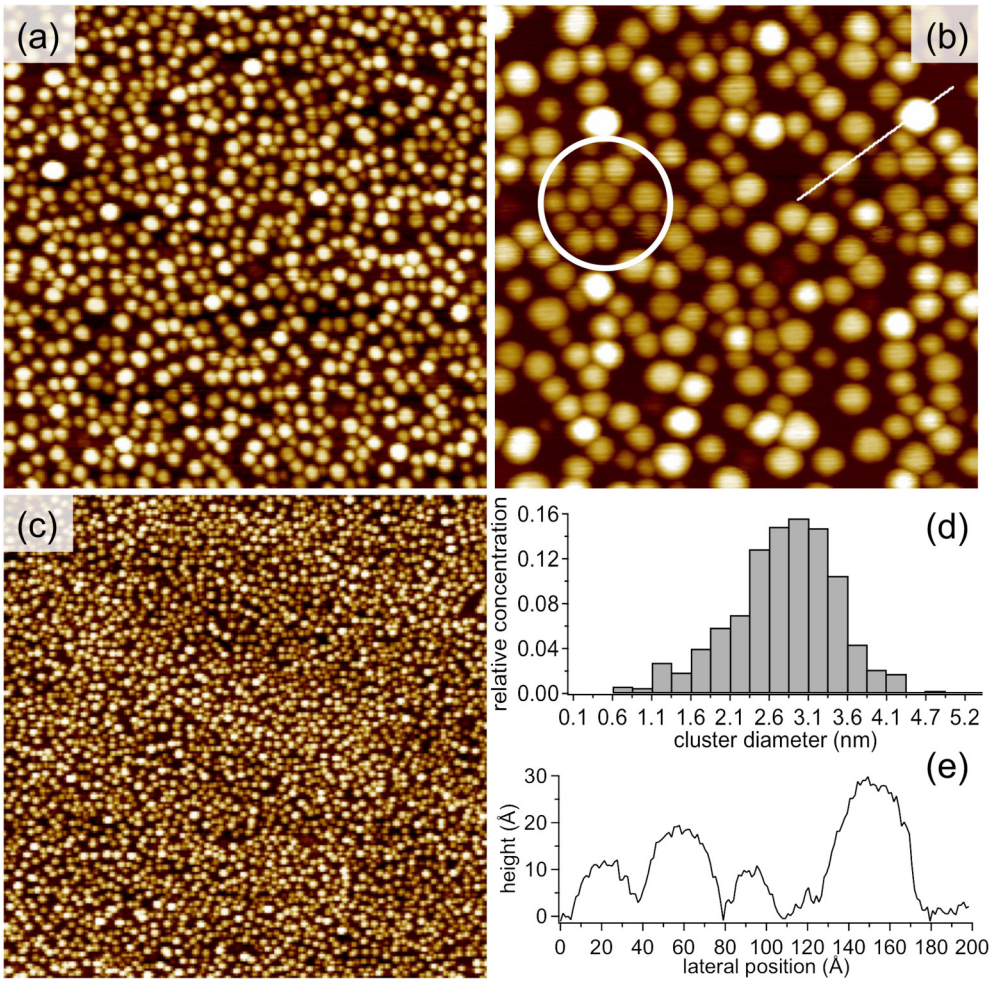

FIG. 5. (Color online) (a) 5 ML Au/*h*-BN/Rh(111) deposited at 115 K, imaged at 300 K, 1000 × 1000 Å. (b) 5 ML Au/*h*-BN/Rh(111) deposited at 115 K, imaged at 300 K, 500 × 500 Å^2. (The superimposed lines and circle are explained in the text.) (c) 5 ML Au/*h*-BN/Rh(111) deposited at 115 K, imaged at 300 K, 2000 × 2000 Å^2 showing large-scale cluster dispersion. (d) Histogram depicting distribution of Au cluster diameters in (a). (e) Line profile along the line indicated in (b).

and see no evidence of so-called "replica islands"—single-layer islands extending over several pores (or repeat distances of the graphene moiré) that maintain the corrugation of the underlying nanomesh or moiré structure. This suggests that the 2D island morphology previously observed on *h*-BN and graphene is principally controlled by the underlying Ru(0001) rather than the *h*-BN monolayer acting as a template. One possible explanation is the relatively weaker binding between *h*-BN on Rh(111) versus Ru(0001). The lesser degree of hybridization between electronic states of the *h*-BN film and the underlying metal results in a greater decoupling of deposited Au from the underlying metal, resulting in the exclusive growth of clusters rather than 2D islands that attempt to maintain the registry of the transition metal surface.

Having seen that the initial stages of Au cluster growth occur exclusively by nucleation within the *h*-BN pores, it is natural to examine the subsequent growth of clusters covering a larger percentage of the surface. Figure 5 depicts the results of 5 ML Au deposited on *h*-BN/Rh(111) at 115 K, and subsequently warmed to room temperature and imaged. Figures 5(a) and 5(d) show a representative 1000 × 1000 Å area of the sample and a histogram showing the distribution of cluster diameters. The distribution is peaked at approximately 28 Å and shows very few clusters larger than 32 Å across—in other words, virtually no clusters are larger than a single unit cell of the *h*-BN film. (Tip convolution effects likely result in measured cluster diameters that are somewhat larger than the actual values.) The 500 × 500 Å image in Fig. 5(b) and corresponding line scan in Fig. 5(e) show representative heights and diameters of several Au clusters—in general, the line profile shows roughly ellipsoidal clusters, with heights approximately 10–25 Å. The clusters indicated by the white circle in Fig. 5(b) show that the hexagonal spacing is roughly maintained, although again tip effects result in a perceived separation between clusters that is slightly smaller than the width of the nanomesh "wire". Figure 5(c) demonstrates the uniformity of the clusters across a larger (2000 × 2000 Å) region of the *h*-BN film. The number density of clusters imaged in Fig. 5 is approximately 0.08 clusters/nm^2, compared to an ideal value of 0.11 clusters/nm^2 (exactly one cluster per pore), or roughly 70% of the density of a "perfect" cluster distribution. Thus even with Au coverages >1 ML, the *h*-BN template facilitates the growth of dense cluster arrays rather than very large individual clusters.

B. X-ray photoelectron spectroscopy

With XPS, we are able to examine the core-level electronic structure of the h-BN film and the deposited Au nanoparticles as a function of Au dosage. In this way, we may experimentally probe for signs of charge transfer to or from the Au and examine the intrinsic metallic properties of the nanoparticles (examining final-state effects related to core hole screening) as a function of particle size.

Due to instrumental limitations, we are unable to measure XPS spectra of a sample held at 115 K after deposition, so are unable to examine the exclusively single-layer clusters imaged in Fig. 1. Due to overlap between the Rh 4s and Au 4f peaks (the Rh 4s binding energy is 81.4 eV [52], and the peak has a strong tail at higher binding energy overlapping the Au 4$f_{7/2}$ peak), it is clearest to present the Au 4f XPS data (open circles in the figure) as difference spectra, subtracting a spectrum from a freshly made h-BN/Rh(111) sample from the Au-dosed spectra to remove the Rh 4s peak. Additional linear backgrounds have been subtracted from the difference spectra and from the single-crystal reference spectrum before fitting. The Rh-derived peaks in all of our spectra show no significant changes as a function of Au dosage other than attenuation. In light of the above observation of a lack of "replica islands" as seen for Au/h-BN/Ru(0001), this may be taken as another indication of a very weak or nonexistent interaction between the Au and the Rh underlying the h-BN film.

The bottommost spectrum in Fig. 6 shows Au 4f XPS from 0.16 ML Au deposited at 115 K and subsequently warmed to room temperature (as imaged in Fig. 3). The best fit to the data is obtained by fitting the Au 4f lines with two pairs of peaks with the appropriate spin-orbit splitting, indicated by the dashed curves in the figure. With reference to an Au single crystal measured in the same XPS system (topmost spectrum in Fig. 6), the binding energy for the more intense peak is shifted slightly higher (0.2 eV), and the less intense peak is shifted considerably higher (0.9 eV). If attributed to an initial state effect, this would suggest that some of the Au clusters are positively charged, but in light of the B 1s and N 1s data presented in Fig. 7 as well as the DFT results presented below, we instead attribute this shift to final-state effects, with reduced screening in the reduced-dimensional Au clusters causing a shift to higher apparent binding energy. We therefore attribute the less intense Au 4f peaks (at 84.76 and 88.46 eV) to the single-layer Au clusters imaged in Fig. 3, and the more intense set of peaks to the bilayer clusters. Supporting this interpretation is the fact that the spectra are best fit with peaks of a Gaussian/Lorentzian product functional form rather than an asymmetric Doniach-Sunjic form characteristic of bulk metallic systems or of nanoparticles large enough to show bulklike screening properties [53].

In light of this interpretation of peak shifts due to final-state effects and multiplets arising from nanoparticles of distinctly different sizes, we can consistently explain all the features of the spectra in Fig. 6. The second spectrum from the bottom, corresponding to 0.16 ML Au deposited and imaged at room temperature (imaged in Fig. 3), shows a similar structure, but with relatively less intensity in the higher binding energy peak and with both peaks shifted to somewhat lower binding energy with respect to that for 0.16 ML Au deposited at 115 K. This suggests that the larger clusters observed in STM after room temperature deposition show some evolution toward more bulklike electronic structure, with the very smallest single-layer clusters still present contributing the higher binding energy component. We still obtain better fits using pairs of symmetric peaks (Gaussian/Lorentzian products) rather than asymmetric (Doniach-Sunjic) line shapes characteristic of metallic Au, which again is consistent with the observed size distribution. In contrast, the spectrum from 5 ML Au deposited at 115 K and measured at room temperature (RT), corresponding to Fig. 5, fits an asymmetric line shape extremely well, with only a very small symmetric component at higher binding energy, again presumably corresponding to nanoparticles at the smaller end of the size distribution. The only deviation from bulklike behavior in the dominant component in the 5 ML Au spectrum is again a small (0.2 eV) shift toward lower binding energy with respect to bulk Au. Given that the clusters deposited under these conditions are overwhelmingly several layers tall and several Å in diameter, final-state effects are not likely to play a large role in the observed peak shift, and the shift to lower binding energy

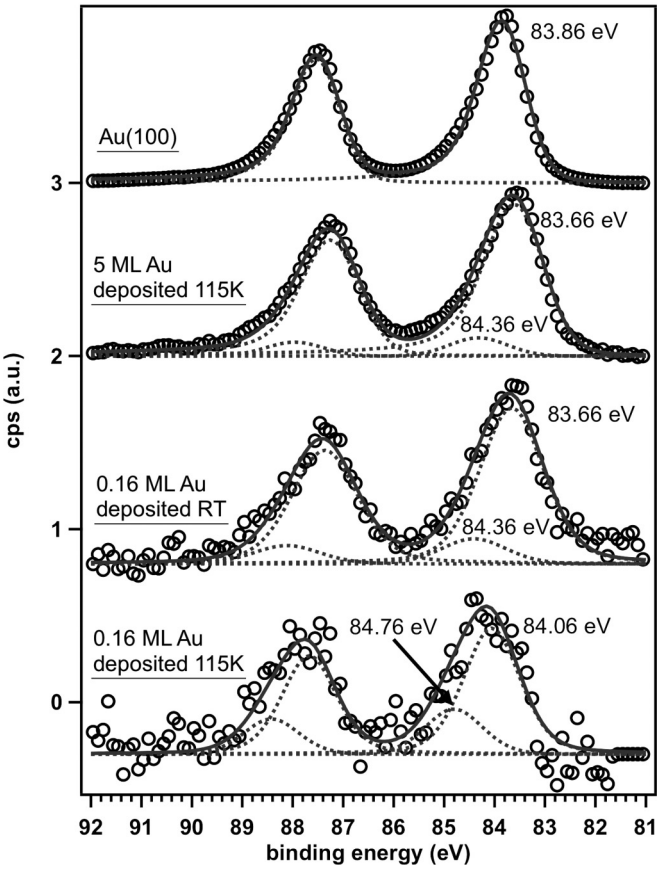

FIG. 6. Au 4f difference XPS with fits. From bottom to top, we show 0.16 ML Au deposited at 115 K, 0.16 ML Au deposited at RT, 5 ML Au deposited at 115 K, and an Au(100) single crystal for reference. All spectra were acquired at room temperature. Open circles show the difference spectra resulting from subtracting a pristine h-BN/Rh(111) spectrum from each Au-dosed spectrum, individual fit components are shown as dashed lines, and overall fit envelopes are shown as solid lines.

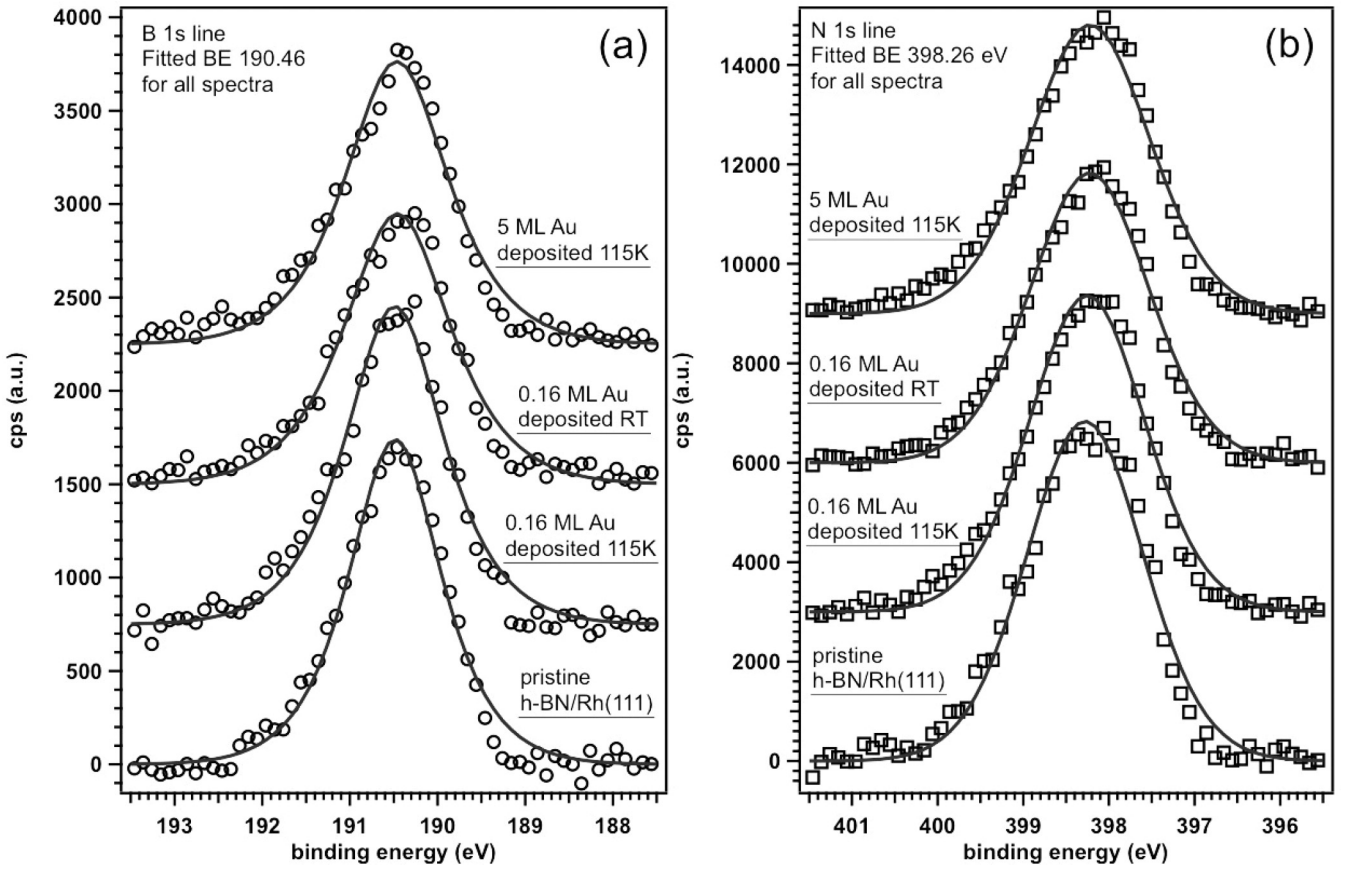

FIG. 7. (a) B 1*s* XPS after the Au doses depicted in Fig. 4. (b) N 1*s* XPS after the Au doses depicted in Fig. 4.

is consistent with a small negative charge residing on the Au clusters. This would be consistent with the results of our Bader charge analysis presented in Sec. V below.

Figures 7(a) and 7(b) show B 1*s* and N 1*s* XPS spectra, respectively, which give some insight into charge transfer between the *h*-BN support and the deposited Au. The bottommost spectrum in each panel shows a freshly prepared *h*-BN film just after film deposition, and subsequent spectra, appropriately labeled, show spectra corresponding to each Au dose imaged in Figs. 3–5. Both B 1*s* and N 1*s* are fit well with a single symmetric peak at binding energies of 190.46 and 398.26 eV, respectively. These are nearly identical to binding energies (referenced to the Fermi level) reported for BN films on Pd(111) [29], and agree within at most ±1.2 eV with binding energies reported for BN on Ni(111), Pt(111), and Ru(0001) [17,29]. Synchrotron XPS experiments have indicated that both the B and N 1*s* peaks are split into two components with a small separation in energy (approximately 0.4 and 0.7 eV, respectively) [22] due to the differing chemical environments of the pores and wires of the nanomesh structure, exactly analogous to the splitting of σ and π bands in valence band photoemission [20]. The reduced resolution, surface sensitivity, and photon flux of laboratory XPS compared to a synchrotron experiment results in the apparent single-peak structure here. Au deposition induces no chemical shift in either peak, and minimal linewidth broadening or narrowing.

We therefore are confident in our interpretation of the Au 4*f* XPS in Fig. 6 as being dominated by final-state effects related to the reduced screening of core holes induced by the restricted nanoparticle size, especially at low coverage. The DFT results discussed below suggest that particularly the single-layer Au clusters do become negatively charged, but the amount of charge transfer from the BN film as reflected in chemical shifts or additional B and N core-level peaks is beyond our ability to detect with laboratory XPS. The STM data presented in Figs. 2–4 above show that the vast majority of the surface remains uncovered by Au at submonolayer coverages, so the percentage of available B or N sites from which charge could be transferred is correspondingly small. The already low cross sections for B 1*s* and N 1*s* at the available photon energy combined with the fraction of a monolayer of atomic sites participating in charge transfer therefore likely renders chemical shifts in these peaks invisible to this experiment regardless of whether they actually occur. A prior extended x-ray-absorption fine structure study of the N *K* edge after 0.2 ML Au deposition on *h*-BN/Rh(111) showed no change in line shape from a clean *h*-BN film either at room temperature or after annealing up to 600 °C, indicating that if charge transfer to Au happens at room temperature, it is likely that charge is primarily transferred from boron [38]. This is consistent with the result one would expect from a simple electronegativity argument.

C. DFT results

We have performed DFT calculations for a series of Au clusters, including Au_1, Au_7, Au_{19}, Au_{30}, Au_{37}, and Au_{51} on

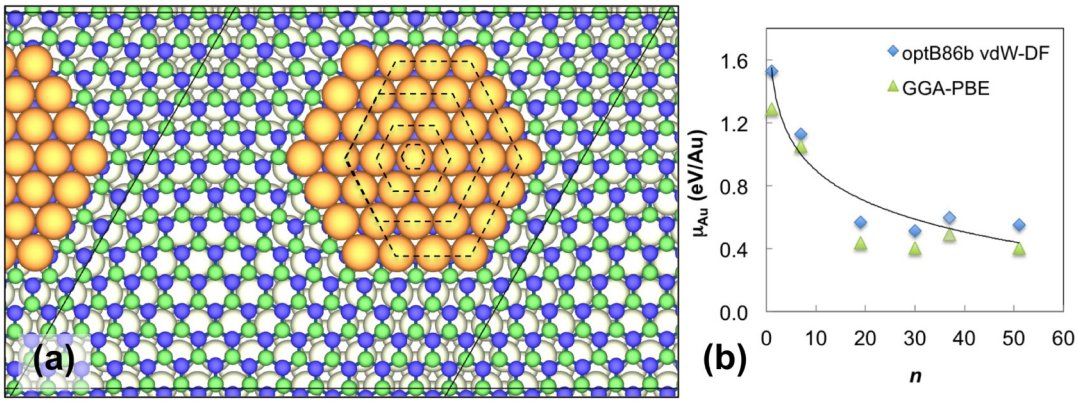

FIG. 8. (Color online) (a) Positions of the $Au_{1,7,19,30,37}$ clusters inside the pore region of the *h*-BN/Rh(111) nanomesh structure. Au_{37} is shown as is, and the successively smaller hexagons outlined by dashed lines indicate the positions of the smaller clusters. White, green, blue, and yellow spheres represent Rh, B, N, and Au atoms, respectively. (b) Calculated Au chemical potential ($\widetilde{\mu}_{Au}$) vs number of atoms in the Au cluster (n). Curve in (b) is a logarithmic function fitted to the optB86b vdW-DF data as a guide to the eye.

13-on-12 *h*-BN/Rh(111) to explore trends in the energetic, electronic, and structural properties of Au clusters on *h*-BN/Rh(111) as a function of size. The multiatom clusters up to Au_{37} were modeled as flat single-layer clusters on account of the STM images described in Sec. III A. We tested the adsorption of an Au adatom at sixfold-symmetry locations at the center of the pore region (atop B) and the wire region (atop N). Consistent with previous reports [39] the center of the pore region is more stable for Au adsorption than the center of the wire region by 1.5 eV. Thus all of the Au clusters are placed centered in the pore region [see Fig. 8(a)]. The average Au chemical potential ($\widetilde{\mu}_{Au}$) as a function of cluster size is plotted in Fig. 8(b). Here $\widetilde{\mu}_{Au}$ for a cluster is defined to be $(E-E')/(n-n')-E_{Au(s)}$, where E and n are the DFT total energy and size of the cluster, and E' and n' are those of the cluster one size smaller in the series studied, and $E_{Au(s)}$ is the energy of bulk Au. Vibrational contributions to the chemical potential are ignored at the low temperature. For monolayer Au clusters it decreases monotonically as more Au atoms are added to the cluster [54] until Au_{37}, where $\widetilde{\mu}_{Au}$ begins to increase. Instead a bilayer Au_{51} cluster (Fig. 9) has a lower $\widetilde{\mu}_{Au}$ (defined with respect to Au_{30}, not Au_{37}) than Au_{37}. This suggests that the further growth of a monolayer Au cluster beyond ~30 atoms is thermodynamically unfavorable and the cluster would transition to bilayer [55], so long as the kinetic barrier for periphery Au atoms that are up against the pore walls to move on top of the bottom Au layer is surmountable

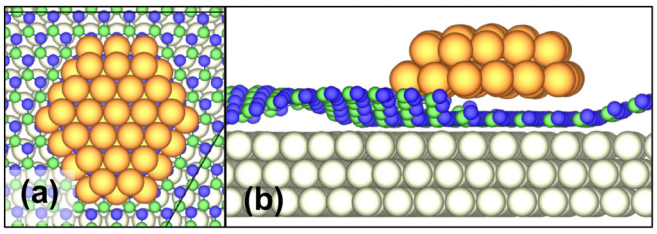

FIG. 9. (Color online) Top view (a) and side view (b) of the bilayer Au_{51} cluster inside the *h*-BN nanomesh pore region. White, green, blue, and yellow spheres represent Rh, B, N, and Au atoms, respectively.

at the substrate temperature. Note that at 0.16 ML deposition coverage, the average number of Au atoms per BN pore is $144 \times 0.16 \approx 23$ assuming even deposition across the surface, so we conclude that the monodisperse Au clusters that formed at 115 K by depositing 0.16 ML of Au on *h*-BN/Rh(111) were predominantly single layer in height. This is consistent with the low-temperature STM results presented in Fig. 2 above.

Bader charge analysis for the clusters shown in Fig. 8 shows appreciable charge transfer to the Au clusters (Table I), which is particularly significant for the monolayer Au_{30} cluster. The addition of a second layer results in less negative charge transferred to Au, both in terms of total charge on the cluster and the average charge per Au atom. Our analysis shows that the topmost layer of the Au_{51} cluster, in particular, is almost neutral. In the absence of strong final-state effects, negatively charged Au clusters should result in the Au 4*f* XPS peaks being shifted to lower binding energy (due to increased Coulomb repulsion of the emitted photoelectron) with respect to the same peaks from a bulk Au crystal, but in Fig. 5 above we observe instead a shift to higher binding energy. This cannot be taken as a sign that no charge transfer has occurred, but rather merely an indication that final-state effects due to reduced particle size are what dominate the experimentally measured spectra for submonolayer coverages. The observed small shift of Au 4*f* peaks to lower binding energy for the 5 ML dosed sample may indicate that a small negative charge on the Au persists even for very large clusters.

We next interrogate the structures of the *h*-BN surface and the Au clusters formed in the pore. The 13-on-12 monolayer *h*-BN pore-wire structure is calculated to have a maximum geometric corrugation (d_{max}, defined to be the height difference between the highest and lowest atoms in the BN structure; cf. Fig. 1) of 2.647 Å (LDA), 2.204 Å (GGA-PBE), and 2.385 Å (optB86b vdW-DF), all of which are significantly greater than the 0.5 Å corrugation measured with STM. With respect to clean BN/Rh(111), the monolayer Au_{30} cluster has a maximum geometric height (the difference between the highest Au atom and lowest atom in the BN structure; cf. Fig. 9) of 3.519/3.489 Å, whereas for Au_{51} it is 7.117/6.277 Å (GGA-PBE/optB86b vdW-DF), which also overestimate the respective 1.5 and 3 Å in STM, respectively

TABLE I. Summary of Bader charge (in electrons, e) and adsorption energies (in eV) of the Au clusters on h-BN/Rh(111). Results based on optB86b vdW-DF.

	Total charge on Au cluster (e)	Average charge per Au atom (e)	Total charge on h-BN monolayer (e)	ΔE (eV)
BN/Rh(111)	n/a	n/a	−1.371	n/a
Au_1/BN/Rh(111)	−0.462	−0.462	−1.107	+1.592
Au_7/BN/Rh(111)	−1.306	−0.187	−0.846	+1.184
Au_{19}/BN/Rh(111)	−2.207	−0.116	−0.318	+0.794
Au_{30}/BN/Rh(111)	−2.543	−0.085	+0.221	+0.691
Au_{51}/BN/Rh(111)	−2.142	−0.042	−0.199	+0.632

(Figs. 2–4). The average interlayer separation in the Au_{51} cluster is 2.783/2.600 Å (GGA-PBE/optB86b vdW-DF). The large difference between the measured and calculated nanomesh corrugation and Au cluster heights is unlikely due to the choice of exchange-correlation functional. The apparent heights measured by STM may feature substantial contributions from tip and substrate electronic structures that cause them to differ from the geometric heights of the pore-wire corrugation and the Au clusters formed in the pore regions.

IV. CONCLUSIONS

We have studied the nucleation and growth of Au clusters on the h-BN/Rh(111) surface using STM, XPS, and DFT. Deposition of submonolayer amounts of Au results in mostly single-layer and bilayer Au clusters confined to the pores of the h-BN nanomesh, with the principal difference between deposition at 115 and 300 K being the change in relative proportion of monolayer and bilayer clusters formed, with monolayer clusters predominating at the lower temperature. Deposition of larger amounts of Au results in the formation of well-dispersed clusters mainly <30 Å across and <25 Å tall, with cluster diameters restricted by the pores of the nanomesh. XPS results show strong influence of final-state effects for submonolayer doses of Au, with suggestions of negative charging of bilayer and larger clusters. DFT calculations demonstrate the size threshold of the monolayer/bilayer transition that is consistent with the STM observations, and provide insight into the distribution of the negative charge on the various monolayer and bilayer clusters. These well-dispersed, negatively charged Au nanoclusters with a relatively narrow distribution of diameter and height suggest that the clusters formed in the present study should show catalytic activity for CO oxidation. The difference in cluster growth modes with respect to Au deposited under similar conditions on h-BN/Ru(0001) and graphene/Ru(0001) (exclusively 3D clusters rather than 2D islands maintaining the nanomesh corrugation) suggests that the Au and h-BN cannot be considered free or pseudo-free; the underlying metal substrate plays a role in determining the Au morphology and thus the catalytic activity.

ACKNOWLEDGMENTS

This material is based upon work supported as part of the Center for Atomic Level Catalyst Design, an Energy Frontier Research Center funded by the US Department of Energy, Office of Science, Office of Basic Energy Sciences under Award No. DE-SC0001058. This research used resources of the National Energy Research Scientific Computing Center, which is supported by the Office of Science of the U.S. Department of Energy under Contract No. DE-AC02-05CH11231.

[1] B. Hammer and J. K. Nørskov, Nature (London) **376**, 238 (1995).
[2] M. Valden, X. Lai, and D. W. Goodman, Science **281**, 1647 (1998).
[3] M. Haruta, Catal. Today **36**, 153 (1997).
[4] M. Haruta, N. Yamada, T. Kobayashi, and S. Ijima, J. Catal. **115**, 301 (1989).
[5] M. Haruta, S. Tsubota, T. Kobayashi, H. Kageyama, M. J. Genet, and B. Delmon, J. Catal. **144**, 175 (1993).
[6] D. W. Goodman, Catal. Lett. **99**, 1 (2005).
[7] N. Spiridis, R. P. Socha, B. Handke, J. Haber, M. Szczepanik, and J. Korecki, Catal. Today **169**, 24 (2011).
[8] M. Amft and N. V. Skorodumova, Phys. Rev. B **81**, 195443 (2010).
[9] J. Guzman and B. C. Gates, J. Am. Chem. Soc. **126**, 2672 (2004).
[10] Z. Yang, R. Wu, Q. Zhang, and D. W. Goodman, Phys. Rev. B **65**, 155407 (2002).
[11] X.-Q. Gong, A. Selloni, O. Dulub, P. Jacobson, and U. Diebold, J. Am. Chem. Soc. **130**, 370 (2008).
[12] L. B. Vilhelmsen and B. Hammer, Phys. Rev. Lett. **108**, 126101 (2012).
[13] M. Corso, W. Auwärter, M. Muntwiler, A. Tamai, T. Greber, and J. Osterwalder, Science **303**, 217 (2004).
[14] A. Goriachko, A. A. Zakharov, and H. Over, J. Phys. Chem. C **112**, 10423 (2008).
[15] W. Auwärter, T. J. Kreutz, T. Greber, and J. Osterwalder, Surf. Sci. **429**, 229 (1999).
[16] R. Laskowski, P. Blaha, T. Gallauner, and K. Schwarz, Phys. Rev. Lett. **98**, 106802 (2007).
[17] A. Goriachko, Y. He, M. Knapp, H. Over, M. Corso, T. Brugger, S. Berner, J. Osterwalder, and T. Greber, Langmuir **23**, 2928 (2007).
[18] A. B. Preobrajenski, A. S. Vinogradov, and N. Mårtensson, Surf. Sci. **582**, 21 (2005).

[19] R. Laskowski, P. Blaha, and K. Schwarz, Phys. Rev. B **78**, 045409 (2008).
[20] A. B. Preobrajenski, S. A. Krasnikov, A. S. Vinogradov, M. L. Ng, T. Käämbre, A. A. Cafolla, and N. Martensson, Phys. Rev. B **77**, 085421 (2008).
[21] R. Laskowski and P. Blaha, Phys. Rev. B **81**, 075418 (2010).
[22] A. B. Preobrajenski, A. S. Vinogradov, M. L. Ng, E. Cavar, R. Westerström, A. Mikkelsen, E. Lundgren, and N. Mårtensson, Phys. Rev. B **75**, 245412 (2007).
[23] A. B. Preobrajenski, M. A. Nesterov, M. L. Ng, A. S. Vinogradov, and N. Mårtensson, Chem. Phys. Lett. **446**, 119 (2007).
[24] A. B. Preobrajenski, A. S. Vinogradov, and N. Mårtensson, Phys. Rev. B **70**, 165404 (2004).
[25] N. Lopez, T. V. W. Janssents, B. S. Clausen, Y. Xu, M. Mavrikakis, T. Bligaard, and J. K. Nørskov, J. Catal. **223**, 232 (2004).
[26] L. M. Molina and B. Hammer, Phys. Rev. Lett. **90**, 206102 (2003).
[27] I. X. Green, W. Tang, M. Neurock, and J. T. Yates, Science **333**, 736 (2011).
[28] R. Laskowski and P. Blaha, J. Phys. Condens.: Matter **20**, 064207 (2008).
[29] A. Nagashima, N. Tejima, Y. Gamou, T. Kawai, and C. Oshima, Phys. Rev. Lett. **75**, 3918 (1995).
[30] A. Goriachko, Y. B. He, and H. Over, J. Phys. Chem. C **112**, 8147 (2008).
[31] J. Zhang, V. Sessi, C. H. Michaelis, I. Brihuega, J. Honolka, K. Kern, R. Skomski, X. Chen, G. Rojas, and A. Enders, Phys. Rev. B **78**, 165430 (2008).
[32] I. Brihuega, C. H. Michaelis, J. Zhang, S. Bose, V. Sessi, J. Honolka, M. Alexander Schneider, A. Enders, and K. Kern, Surf. Sci. **602**, L95 (2008).
[33] A. T. N'Diaye, T. Gerber, C. Busse, J. Mysliveček, J. Coraux, and T. Michely, New J. Phys. **11**, 103045 (2009).
[34] B. F. Habenicht, D. Teng, L. Semidey-Flecha, D. S. Sholl, and Y. Xu, Top. Catal. **57**, 69 (2013).
[35] B. F. Habenicht, Y. Xu, and L. Liu, *Theoretical Perspectives* (Wiley, Chichester, UK, 2013), pp. 425–446.
[36] L. Liu, Z. Zhou, Q. Guo, Z. Yan, Y. Yao, and D. W. Goodman, Surf. Sci. **605**, L47 (2011).
[37] Y. Xu, L. Semidey-Flecha, L. Liu, Z. Zhou, and D. Wayne Goodman, Faraday Discuss. **152**, 267 (2011).
[38] M. L. Ng, A. B. Preobrajenski, A. S. Vinogradov, and N. Mårtensson, Surf. Sci. **602**, 1250 (2008).
[39] H. P. Koch, R. Laskowski, P. Blaha, and K. Schwarz, Phys. Rev. B **84**, 245410 (2011).
[40] H. P. Koch, R. Laskowski, P. Blaha, and K. Schwarz, Phys. Rev. B **86**, 155404 (2012).
[41] R. Q. Hwang, J. Schröder, C. Günther, and R. J. Behm, Phys. Rev. Lett. **67**, 3279 (1991).
[42] G. Kresse and J. Furthmuller, Phys. Rev. B **54**, 11169 (1996).
[43] J. P. Perdew, K. Burke, and M. Ernzerhof, Phys. Rev. Lett. **77**, 3865 (1996).
[44] J. Klimeš, D. R. Bowler, and A. Michaelides, Phys. Rev. B **83**, 195131 (2011).
[45] J. Klimeš, D. R. Bowler, and A. Michaelides, J. Phys.: Condens Matter **22**, 022201 (2009).
[46] G. Kresse and D. Joubert, Phys. Rev. B **59**, 1758 (1999).
[47] M. Methfessel and A. Paxton, Phys. Rev. B **40**, 3616 (1989).
[48] N. W. Ashcroft and N. D. Mermin, *Solid State Physics* (Saunders College, Rochester, 1976).
[49] J. Neugebauer and M. Scheffler, Phys. Rev. B **46**, 16067 (1992).
[50] R. F. W. Bader, *Atoms in Molecules—A Quantum Theory* (Oxford University Press, Oxford, 1990).
[51] G. Henkelman, A. Arnaldsson, and H. Jónsson, Comput. Mater. Sci. **36**, 354 (2006).
[52] *X-Ray Data Booklet*, 2nd ed., edited by A. C. Thompson and D. Vaughan (Lawrence Berkeley National Laboratory, Berkeley, CA, 2001).
[53] S. Doniach and M. Sunjic, J. Phys. C **3**, 285 (1970).
[54] C. T. Campbell, Acc. Chem. Res. **46**, 1712 (2013).
[55] P. J. Feibelman, Phys. Rev. B **80**, 085412 (2009).